



Aero-manufacture of nanobulges for an in-place anticoronaviral on air filters

Jisoo Choi^{a,1}, Kishwor Poudel^{b,c,1}, Kang Sik Nam^{a,1}, Amin Piri^a, Adriana Rivera-Piza^d, Sae Kwang Ku^e, Jungho Hwang^{a,*}, Jong Oh Kim^{b,*}, Jeong Hoon Byeon^{f,*}

^a School of Mechanical Engineering, Yonsei University, Seoul 03722, Republic of Korea

^b College of Pharmacy, Yeungnam University, Gyeongsan 38511, Republic of Korea

^c Wellman Center for Photomedicine, Department of Dermatology, Meassachusetts General Hospital, Harvard Medical School, MA 02114, USA

^d Department of Biotechnology, Korea University, Seoul 02841, Republic of Korea

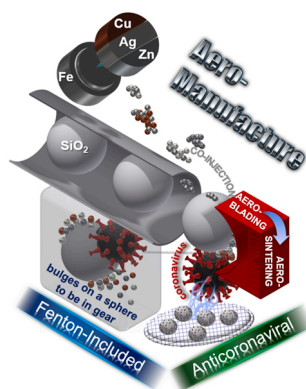
^e College of Korean Medicine, Daegu Haany University, Gyeongsan 38610 Republic of Korea

^f School of Mechanical Engineering, Yeungnam University, Gyeongsan 38541, Republic of Korea

HIGHLIGHTS

- An in-flight nanobulge manufacture was developed to confer antivirals in-place.
- Human coronaviruses on the filter were inactivated while retaining biosafety.
- The Fenton-mediated reactions from nanobulges resulted in comparable antivirals.

GRAPHICAL ABSTRACT



ARTICLE INFO

Editor: <Dr. Danmeng Shuai>

Keywords:

Antiviral air filter
Coronavirus infection
In-place antiviral coating
Electrically operable dispenser
Bimetallic bulge structure

ABSTRACT

The interest in removing contagious viruses from indoor air using ventilation and filtration systems is increasing rapidly because people spend most of the day indoors. The development of an effective platform to regenerate the antiviral function of air filters during use and safe abrogation of used filters containing infectious viruses is a challenging task, because an on-demand safe-by-design manufacture system is essential for in-place antiviral coatings, but it has been rarely investigated. With these considerations, an electrically operable dispenser was prepared for decorating continuous ultrafine Fe–Zn, Fe–Ag, or Fe–Cu particles (<5 nm) onto SiO₂ nanobeads (ca. 130 nm) to form nanobulges (*i.e.*, nanoroughness for engaging coronavirus spikes) in the aerosol state for 3 min direct deposition on the air filter surfaces. The resulting nanobulges were exposed to human coronaviruses (HCoV; surrogates of SARS-CoV-2) to assess antiviral function. The results were compared with similar-sized

* Corresponding authors.

E-mail addresses: hwangjh@yonsei.ac.kr (J. Hwang), jongohkim@yu.ac.kr (J.O. Kim), postjb@yu.ac.kr (J.H. Byeon).

¹ These authors contributed equally.

individual Zn, Ag, and Cu particles. The nanobulges exhibited comparable antiviral activity to Zn, Ag, and Cu particles while retaining biosafety in both *in vitro* and *in vivo* models because of the significantly smaller metallic fractions. This suggests that the bimetallic bulge structures generate reactive oxygen species and Fenton-mediated hydroxyl radicals for inactivating HCoV.

1. Introduction

Humans spend almost 90 % of their day indoors. Hence, indoor air quality management has been a critical issue for human health, even before the coronavirus outbreak (SARS-CoV-2) (Shen et al., 2021a; Sunday and Sakugawa, 2020). In this connection, mechanical ventilation and wearing a mask are strongly recommended as a simple and efficient way of suppressing the airborne transmission of coronaviruses (Cheng et al., 2021; Hadei et al., 2021; Wang et al., 2021). Maintaining these non-pharmaceutical interventions is essential for returning to back-to-normal after vaccination for most people because of the resurgence of SARS-CoV-2 infections based on viral evolution (Annavaiah et al., 2021; Jones et al., 2021; Shen et al., 2021a). On the other hand, the distribution of the air in which the coronavirus is present through air conditioning (*i.e.*, circulating coronavirus-laden air) and the inappropriate use of masks (*i.e.*, fomite mediated infection) may cause another form of coronavirus transmission (Correia et al., 2020; Mouchtouri et al., 2020; Park et al., 2021a). These potential risks highlight the need for adequate filtration in indoor air because there are significant leakages of exhaled air during wearing masks (Bazzazpour et al., 2021; Curtius et al., 2021; Radney et al., 2021; Shen et al., 2021b; Zacharias et al., 2021).

The removal of airborne viruses and particulate matter (PM), including those by air filtration, includes inertial impaction, interception, diffusion, and electrostatic attraction of PM to attach to a nonwoven surface (Tian et al., 2021). On the other hand, the attached viruses on the surface can survive more than seven days, which may cause a problem of the release of infectious viruses from filters in use or discarded after use (Balagna et al., 2021; Christopherson et al., 2020; Huang et al., 2020; Li et al., 2021; Nazarenko, 2020). As an alternative to prevent this, strategies for inhibiting the growth of viruses attached to the filter surface by coating the surface with an antimicrobial agent or installing a germicidal lamp around the filter have been suggested (Elsaid and Ahmed, 2021; Horváth et al., 2020; Kwon et al., 2021; Siddiqui et al., 2020; Sodi et al., 2021; Wu et al., 2021). On the other hand, there are critical issues in performance deterioration of antimicrobial nanoparticle coatings due to the blockage by PM collection during use and possible nanoparticle toxicity and fire risk due to the photothermal effect of the nanoparticles (Jazie et al., 2021; Kwon et al., 2021; Li et al., 2021; Valiei et al., 2020; Zhu et al., 2021). In the case of installing germicidal lamps, there are critical issues in high energy consumption with a limited virucidal effect on the depth direction of the deep-bed filters and the degradation of filter materials caused by ultraviolet light exposure (Agarwal et al., 2021; Malloy et al., 2021; Sleiti et al., 2021). Therefore, an on-demand dispenser accessible from the outside exhibiting safe-by-design and stable antiviral activity that is combinable with air filters are needed to prevent virus transmission through indoor air conditioning and release from the filters after use for securing rapid implementation, electrical operation, affordability, and biosafety (Fan et al., 2021; Macfarlane, 2021; Sellaoui et al., 2021).

In this study, an electrically operable aerosol dispenser was designed and constructed, and the resulting particles were collected to assess the anticoronaviral activity and biosafety. In particular, SiO₂ nanobeads (*ca.* 130 nm; to cover even the largest size of HCoV (about 80–120 nm in diameter) (Liu et al., 2021a)) were decorated with bimetallic (Fe–Zn, Fe–Ag, or Fe–Cu) ultrafine particles (<5 nm) in-flight to construct nanobulges that generate anticoronaviral nanoroughness on a biocompatible SiO₂ surface for engaging coronavirus spikes (Häffner et al., 2021; Liu et al., 2021b; Nie et al., 2020) while minimizing the Zn, Ag, or

Cu content (broad-spectrum antimicrobial and essential elements (Ermini and Voliani, 2021; Pal et al., 2021; Stabryla et al., 2021) but potentially toxic (Hodek et al., 2016; Imani et al., 2020; Neal et al., 2021)). Unlike our previous studies used directly microbiocidal Ag (Joe et al., 2014; Park et al., 2019a, 2021b), Fe was selected to compensate for the anticoronaviral activity of individual Zn, Ag, or Cu through Fenton-mediated radical generation and restrain the toxicity of the adjacent particles because of its biocompatibility (Barciszewska, 2021; Tao et al., 2020). In this regard, Fe-containing bimetallic nanoparticles have recently shown better antimicrobial activity than the monometallic configurations in biomedical and water treatment applications (Das et al., 2018; Marková et al., 2013; Sathya et al., 2018). The in-flight construction and subsequent supply of nanobulges were streamlined by the plasma ablation of Fe and Zn (or Ag, Cu) rods, vibrating nozzle spray of SiO₂ bead suspension, and electrically heated flow reactor. As shown in Fig. 1, agglomerates consisting of Fe and Zn (or Ag, Cu) from ablation and SiO₂ beads from the spray were coinjected into an orifice to redistribute the agglomerates into singlet particles on the beads (*i.e.*, aero-blading from shattering effect) (Byeon and Roberts, 2012) to form nanobulges (Fe–Zn, Fe–Ag, or Fe–Cu by replacing the metal–metal rod configuration for ablation). The nanobulges were then passed through a heated flow tube reactor to sinter the singlet particles for potent binding to the beads (*i.e.*, aero-sintering) in a single-pass in-flight configuration. The nanobulge coating on filter surfaces was achieved by passing the

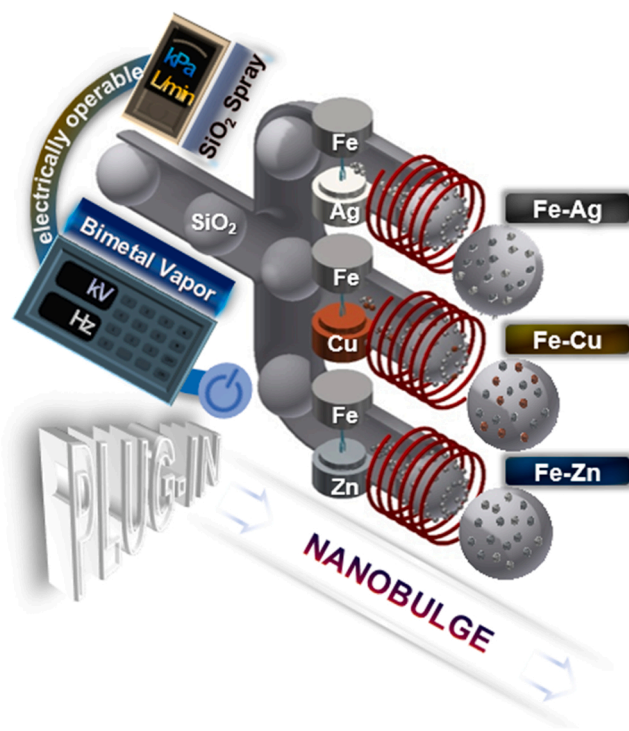


Fig. 1. Illustration of the plug-in manufacture of Fe–Zn, Fe–Ag, and Fe–Cu nanobulges. Coinjection of the vibrating sprayed SiO₂ nanobeads and vapors from the plasma channels between two different metal rods was carried out in the presence of gas flow for combining the nanobeads and bimetallic agglomerates and subsequent thermal curing through an orifice to construct the ultrafine bimetallic particle decorated SiO₂ nanobead. Electrically operable devices were integrated with a duct as a plug-in dispenser for the in-place antiviral functionalization of an air filter.

nanobulge-laden flow directly through a filter inserted holder for mechanical filtration, thereby enabling electrically operable dry functionalization of the filter surfaces. The resulting nanobulges and coated filters (for 3 min deposition) were exposed to human coronavirus (HCoV) 229E and OC43 strains as surrogates of SARS-CoV-2 to examine the anticoronaviral activity (Fig. S1A) as well as mammalian (human dermal fibroblasts (HDF) and lung fibroblasts (WI-38)) cells and BALB/c mice to assess the biosafety (Fig. S1B).

2. Experimental

2.1. Nanobulge manufacture and characterization

SiO₂ nanobeads were decorated with in-flight bimetallic (Fe–Zn, Fe–Ag, or Fe–Cu) particles and assessed for their effects on the antiviral activity. Agglomerates (Fe with Zn, Ag, or Cu) of individual ultrafine particles (<5 nm) produced from the atmospheric-plasma ablation (3 kV, 0.8–2.6 kHz) of Fe and Zn (or Ag, Cu) rods under a 2.37 L min^{−1} N₂ flow and vibrating nozzle-sprayed SiO₂ nanobeads (suspension of commercial mesoporous SiO₂ nanobeads; MKNano, Canada) under 0.63 L min^{−1} O₂ flow were coinjected into an orifice (0.3 mm diameter) to shatter the agglomerates into individual ultrafine particles on the beads (i.e., forming nanobulges through aero-blading) due to a sudden change in gas pressure between the front and rear points of the orifice (Byeon and Roberts, 2012). The nanobulge-laden gas flow was then injected into an electrically heated pipe (400 °C wall temperature because of lower melting points ($\frac{T_m(D_p)}{T_m(Bulk)} = 1 - \frac{6V}{\Delta H_f D_p} [\gamma_{sv} - \gamma_{lv} \left(\frac{\rho_s}{\rho_l}\right)^{1/2}]$), where $T_m(D_p)$ and $T_m(Bulk)$ are the melting temperatures for the ultrafine and bulk metal particles, respectively, and V , ΔH_f , γ_{sv} , γ_{lv} , ρ_s , and ρ_l are the particle volume, bulk heat of fusion, solid–liquid interfacial energy, liquid–vapor interfacial energy, solid density, and liquid density, respectively) to achieve ultrasmall (<5 nm) Fe, Zn, Ag, and Cu bulges for sintering to enhance the bonding strength between the ultrafine particles and nanobeads. The resulting gas flow was directly sampled to measure the in-flight size distribution of nanobulges, which was obtained using a scanning mobility particle sizer (SMPS; 3936, TSI, USA). The zeta potentials of the resulting nanobulges were obtained using Nano-S90 ZetaSizer (Malvern Instruments, UK) after dispersal in deionized water. The particle charge current of aerosol nanobulges was obtained using an aerosol electrometer (Charme®, Palas, Germany). The morphologies of the resulting nanobulges were observed by Transmission electron microscopy (TEM; Tecnai G2 F20 S-TWIN, FEI, USA) and scanning electron microscopy (SEM; S-4800, Hitachi, Japan), while composition and surface state were analyzed by energy-dispersive X-ray (EDX; S-4800, Hitachi, Japan) and X-ray photoelectron spectroscopy (XPS; K-Alpha, Thermo Scientific, USA), respectively. The HCoV-229E exposures to the nanobulge suspension and nanobulge-coated filter were examined by atomic force microscopy (AFM; XE-100, Park Systems, Korea) and SEM (after sputter coating with Au), respectively.

2.2. Antiviral activity

HCoV-229E and -OC43 strains were selected as the surrogates of SARS-CoV-2 to evaluate the anticoronaviral activity of the resulting nanobulges. The resulting nanobulges (Fe–Zn, Fe–Ag, or Fe–Cu), including similar-sized commercial Zn, Ag, or Cu particles (Uninano, Korea) for comparison, were injected into a viral dispersion (2.0×10^5 plaque-forming units (PFU) mL^{−1} for HCoV-229E; 4.2×10^7 PFU mL^{−1} for HCoV-OC43) for aqueous exposure (1 mg mL^{−1}) and then removed after the exposure. In the case of filter exposure, the HCoV-229E viruses were aerosolized using a nebulizer and diffusion dryer in the presence of air flow (2.1 cm/s of face velocity (about half of that in a previous study for air filtration (Orlando et al., 2021)) to reduce viral damage by inertial impaction on fibrous filter media; 24 °C temperature and 40 % relative humidity to follow the guideline (Mousavi et al.,

2021)), and the aerosol HCoV-229E viruses (8.19×10^6 viruses cm^{−3}-air) were directed to the nanobulge coated filter (6.3×10^{-5} g cm^{−2}; 2.8 min is required to achieve this coating density using a single channel nanobulge dispenser) installed in the rectangular duct. A part of the virus-loaded filter was immersed in a conical vial filled with 1 mL of deionized water. The vial was then vibrated using a vortex mixer (KMC-1300V, Vision Scientific, Korea) for 10 min to detach the viruses from the filter. The nanobulge exposure time to the viruses in the aqueous and on the filter was 15 min. The fraction of undamaged RNA of the filter exposed viruses was determined by quantitative real time-polymerase chain reaction (qRT-PCR; 12675885, Thermo Fisher Scientific, UK). The anticoronaviral efficiency was determined using plaque assay, as described elsewhere (Park et al., 2021a). The viral infectivity upon the nanobulge exposure was assessed by infecting the WI-38 cells with HCoV-229E at different MOI with and without the nanobulges, including with individual Zn, Ag, and Cu particles for comparison.

2.3. In vitro cytotoxicity

The cytocompatibility of the resulting Fe–Zn, Fe–Ag, and Fe–Cu nanobulges was assessed in HDF and WI-38 cells through 3-(4,5-dimethylthiazol-2-yl)-2,5-diphenyltetrazolium bromide (MTT) assays. Dulbecco's modified eagle medium (Hyclone, GE Healthcare Biosciences, USA) supplemented with 10% fetal bovine serum and 1 % penicillin–streptomycin, was used to culture the cells in an incubator (37 °C, 5 % CO₂). Approximately 1×10^4 cells per well were seeded in 96-well plates, left to adhere for 24 h, and exposed to different concentrations ($1 - 200 \mu\text{g mL}^{-1}$) of nanobulges for 24 h or 48 h. Subsequently, 100 μL of the MTT reagent (1.25 mg mL^{-1}) was then added to each well and incubated in the dark for 4 h. The formazan crystals formed were dissolved by dimethyl sulfoxide (cell-culture grade, Sigma-Aldrich, USA). The absorbance of the resulting solution was obtained using a microplate reader (Multiskan EX, Thermo Fisher Scientific, USA) at a wavelength of 570 nm.

2.4. In vitro ROS generation

ROS generation in the nanobulge-exposed cells was analyzed using a 2',7'-dichlorodihydrofluorescein diacetate (DCFH-DA) assay (ab113851, Abcam, UK). Approximately 1×10^5 cells per well were seeded on a 12-well plate and incubated overnight. The cells were exposed to nanobulges for 48 h, and then stained with DCFH-DA (30 μM) for 30 min in the dark. The resulting ROS production was identified by a flow cytometry using a fluorescence-activated cell-sorting machine (BD Biosciences, USA).

2.5. Virus-infected cell viability

MRC-5 (human diploid lung fibroblast) cells were cultured in Dulbecco's modified eagle medium (Hyclone, GE Healthcare Biosciences, USA) supplemented with 10 % fetal bovine serum and 1% penicillin–streptomycin in an incubator (37 °C, 5 % CO₂). Approximately 1×10^5 MRC-5 cells per well were seeded on a 96-well plate and incubated overnight. 200 $\mu\text{g mL}^{-1}$ of Fe–Zn, Fe–Ag, and Fe–Cu nanobulges were added to MRC-5 cells for 5 h. HCoV-229E was co-incubated with the nanobulges and cells for 2 h and rinsed to remove the uninternalized viruses. The samples were incubated with 100 μL of CellTiter-Glo® (luminescent cell viability assay kit, Promega, USA) reagent for 1 h. The signals were measured by the multilabel plate reader (VICTORX5, PerkinElmer, USA).

2.6. Caspase-3 activity

Approximately 1×10^5 MRC-5 cells per well were seeded on a 96-well plate and incubated overnight. The cells were exposed to the

nanobulges for 6 h and subsequently infected with HCoV-229E for 2 h. The caspase-3 activity (%) was detected at 30 and 90 min using Caspase-Glo® 3/7 assay system (Promega, USA). The signals were measured by the multilabel plate reader.

2.7. Viral infectivity

Primer specificities for the gene expression were validated using qRT-PCR based melting curve analysis. The levels of mRNA expression were assessed using the Thermo Scientific™ PikoReal™ qRT-PCR system (TCR0096, USA) and THUNDERBIRD™ SYBR® qPCR Mix (Toyobo, Japan). Relative levels of gene expression were calculated through the threshold cycle method and normalized to the reference gene. Thermal cycling conditions were as follows: denaturation at 95 °C for 5 min, followed by 39 cycles of denaturation at 95 °C for 10 s, annealing at 58 °C for 10 s, and extension at 72 °C for 30 s. The melting curve was obtained by heating the amplicon from 65 to 95 °C in a continuous acquisition mode.

2.8. Hemolysis

Blood was cannulated from Sprague-Dawley rats, and the plasma was removed by washing with phosphate-buffered saline (PBS) followed by centrifugation. The harvested red blood cell (RBC) suspension (0.5 mL) was incubated with nanobulges (50, 100, 200, and 400 µg mL⁻¹). The samples were incubated at 37 °C for 8 h and centrifuged (4000 rpm) for 10 min. The absorbance of the supernatants was determined using a UV-Vis spectrophotometer (U-2800; PerkinElmer, USA) at a 540 nm wavelength.

2.9. In vivo toxicity

This assay was conducted by dividing the mice into four different groups, control and three treatment groups (treated with Fe–Zn, Fe–Ag, and Fe–Cu nanobulges). The three treatment groups underwent the intraperitoneal administration (100 mg kg⁻¹) of nanobulges while the control group was treated with saline. The body weights, behavioral changes, and survival rates were recorded for 18 days and the mice were then sacrificed for further examination.

2.10. Histopathological analysis

The vital organs (brain, heart, liver, spleen, lung, and kidney) were harvested from the sacrificed mice from the control and treatment groups. The excised and isolated organs were fixed in neutral buffered formalin (10 %), implanted in paraffin using an automated tissue processor (Shandon Citidel 2000, Thermo Scientific, USA), and the organs (3–4 µm) were sectioned using a microtome (RM2255, Leica Biosystems, Korea). Hematoxylin and eosin staining was conducted on sections of the organs, and an optical microscope (Eclipse 80i, Nikon, Japan) was used for the histopathological examination.

2.11. Biochemical blood analysis

The blood was isolated from the anesthetized mice by a cardiac puncture. On day 18, 1 mL of blood was isolated and centrifuged (3000 rpm) for 15 min to isolate the serum blood for biochemical examination. The hematological parameters (RBC, white blood count (WBC), hemoglobin (HGB), hematocrit (HCT), mean corpuscular volume (MCV), and others) were inspected. The liver (hepatotoxicity) and kidney (nephrotoxicity) functions were determined by analyzing the alkaline phosphatase (ALP)-aspartate transaminase (AST) and blood urea nitrogen (BUN)-creatinine (CRE) serum levels, respectively.

All data are expressed as the mean and standard deviation. The animal handling and experiments were conducted in accordance with the Guidelines for Care and Use of Laboratory Animals and approved by the

Institutional Animal Ethics Committee of Yeungnam University.

3. Results and discussion

The SiO₂ nanobeads decorated with bimetallic singlet particles were identified using an SMPS by comparing the size distributions of the combined (Fe–Zn, Fe–Ag, and Fe–Cu) and individual (bimetallic agglomerate-45.2 nm of average geometric mean diameter (GMD) and SiO₂ nanobead-129.7 nm of individual GMD) components (Fig. S2A). The combined configurations (Fe–Zn (137.0 nm), Fe–Ag (136.4 nm), and Fe–Cu (135.8 nm)) showed similar GMD and geometric standard deviations (GSD) to those of SiO₂ alone while no bands were observed at the region for the agglomerates (Fig. S2A and Table S1). The slight differences in GMD (~6.7 nm) between the combined and individual SiO₂ particles represented the redistribution of agglomerates into singlet particles on the nanobeads. This may be due to the shattering of agglomerates caused by the sudden changes in gas pressure (ΔP) across the orifice ($D_p = \alpha \sqrt{\frac{D_{pa} H}{6\pi \Delta P \theta^2}}$, where α , H , and θ are the proportionality constant, Hamaker constant, and maximum cohesive strength parameter between the constituting particles in an agglomerate, respectively) for aero-blading (Byeon and Roberts, 2012), resulting in a decrease in particle size from 45.2 (D_{pa} -agglomerate size) to 6.7 nm (D_p -shattered particle size). Hence, aero-blading is a workable process for redistributing the bimetallic agglomerates (due to the three orders of magnitude greater particle diffusion coefficient in gas phase than in aqueous solutions) (Feng et al., 2015) into several nanometers on the nanobeads without the use of additional external forces.

The zeta potentials of the collected nanobulges were obtained using a zetasizer after dispersing the nanobulges in deionized water. As shown in Fig. S2B, the nanobulges exhibited negative surface charges over the pH range (3–9), and there were no significant differences between the nanobulges. The negative charges might be due to surface electron losses because plasma ablation (30 kV cm⁻¹ for the present case) causes the transport of accelerated ions and energetic electrons that collide with the adjacent condensed metallic (Fe, Zn, Ag, or Cu) particles. This hypothesis matched the surface chemical states of the metallic particles obtained by XPS in which the spectra of the particles exhibit oxidized states (shifting and distortion for the characteristic bands of binding energies) compared to those of the zero-valent counterparts (Fig. S3). The surface states of the nanobulges may adsorb the negative charges in water electrostatically from the autoionization phenomenon (Egan and Paesani, 2018; Novelli et al., 2019), generating negative polarity in the zeta potential measurement. The negative charge currents of the nanobulges (inset table of Fig. S2B) observed in-flight further supported the surface states that draw negative charges in the gas flow because there was no positron in the experimental gas and air environment (Cheng, 2006). Considering the electrostatic interactions between the coronavirus and oppositely charged surface (Javidpour et al., 2021), the negatively charged nanobulges may confer a binding function to the positively charged spike proteins to perform efficient antiviral action.

TEM was performed on the resulting nanobulges captured upon in-flight direct collection on carbon-coated copper grids during aeromanufacture (Fig. 2). Low-magnification images exhibited a distribution of spherical particles for all nanobulge configurations while the dark dots (<5 nm, mean of 200 particles) on noncrystalline spherical domains (i.e., SiO₂ nanobeads) were obtained in the high-magnification images. Interestingly, no alloyed bulges were detected by TEM; only the characteristic lattice spacings of individual Fe ($d_{Fe, 200} = 0.143$ nm), Zn ($d_{Zn, 101} = 0.242$ nm), Ag ($d_{Ag, 111} = 0.230$ nm), and Cu ($d_{Cu, 111} = 0.209$ nm) were identified in the higher-magnification TEM images. These results may be due to the significant difference in the lattice spacings of Fe and Zn (or Ag, Cu) (Tao et al., 2020) and the rapid quenching of the ablated metal vapors in the presence of gas flow (Byeon and Kim, 2010). According to the antimicrobial activity of the bimetallic nanoparticles in a previous report (Zheng and Xie, 2020), the

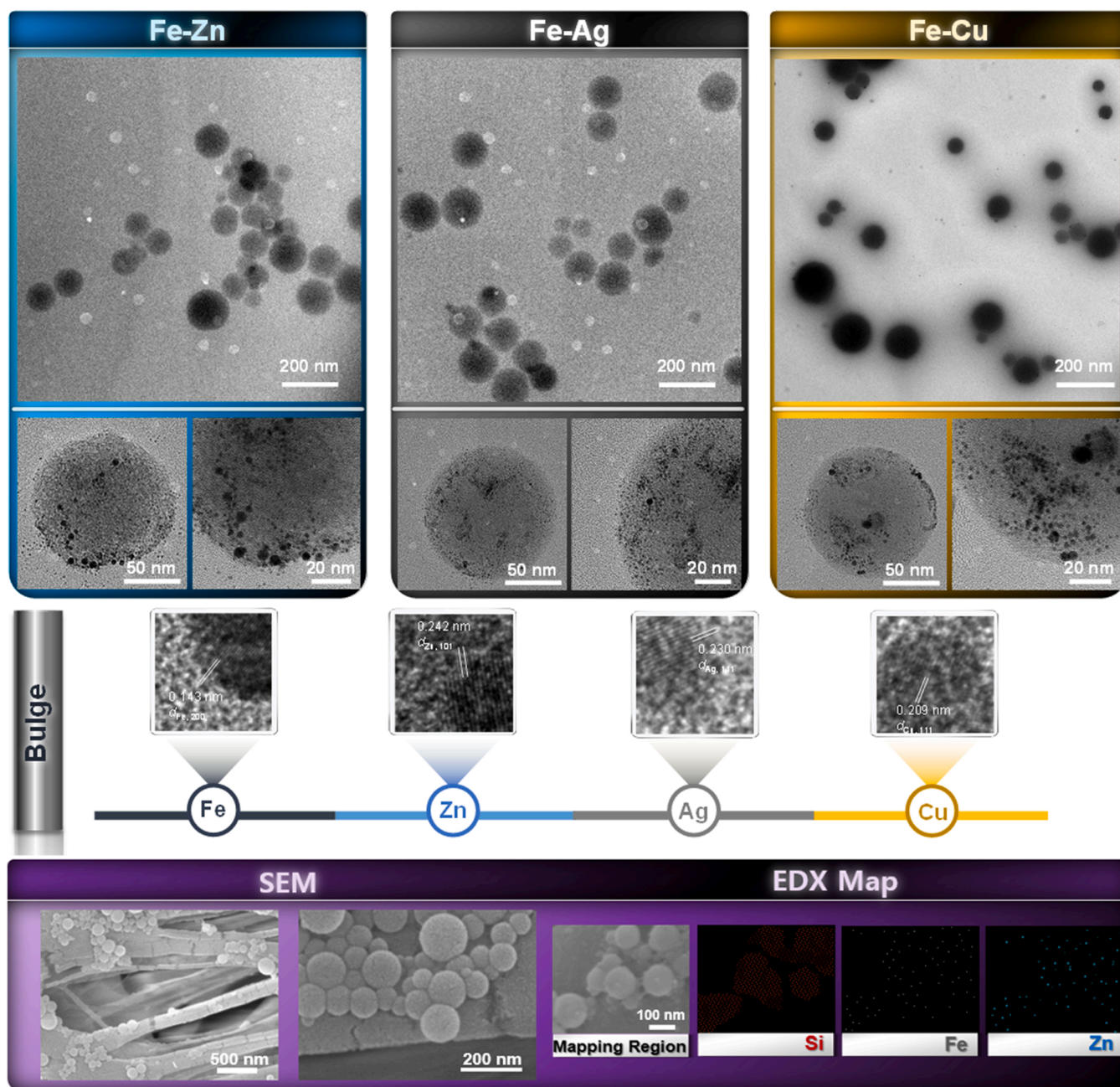


Fig. 2. Morphological and compositional analyses of the resulting particles from the plug-in manufacture. Low- and high-magnification TEM images of Fe–Zn, Fe–Ag, and Fe–Cu are shown as a dark dot distribution on spherical particles. The lattice spacings of the dark dots matched the monometallic Fe, Zn, Ag, and Cu crystals, while noncrystalline characteristics formed in the spherical domains. The representative SEM images and EDX maps of Fe–Zn-coated filter exhibited the distribution of spherical particles on filter fibers, in which elemental dots for Si and Fe–Zn coincide with the main and outer domains of the particles, respectively.

distribution of the individual components (Fe with Zn, Ag, or Cu) to be contacted to HCoV may show significant anticoronaviral activity because of the coupled reactions between the two metals (Weiss et al., 2020). In addition, the bonding strength between the bimetallic particles and SiO_2 nanobeads was even retained after the nanobulges were exposed to bath ultrasonication for 10 min. The in-flight thermal treatment in the heated tube (400 °C wall temperature) may provide strong bindings (sintering effects) between the particles and beads. Representative low- and high-magnification SEM images revealed a collection of the nanobulges on the filter fibers (the bottom of Fig. 2) as the anti-coronaviral coating. The high-magnification image supported the redistribution of bimetallic agglomerates on the nanobeads because none of the beads attached and the satellite agglomerates induced a

nonsmooth surface on the nanobulges (i.e., singlet particles distribution on the beads). The air injection (1.5 m/s face velocity) into a nanobulge coated filter installed rectangular duct did not induce the particle detachment from the filter surface (0.03 particles cm^{-3} was detected downstream of the filter), which may be due to adhesion forces (van der Waals and capillary forces) between the nanobulges and filter surfaces (Park et al., 2021a). EDX elemental maps of Fe–Zn (0.64–0.36 in mass ratio; 0.65–0.35 for both Fe–Ag and Fe–Cu by adjusting the frequency of plasma ablation; Fe–Zn: SiO_2 (0.146:0.854 in mass ratio), Fe–Ag: SiO_2 (0.126:0.874), and Fe–Cu: SiO_2 (0.134:0.866)) confirmed the distribution of Fe and Zn particles on the SiO_2 nanobeads that makes a relatively rough surface effective for engaging HCoV spikes. Fig. S4 shows the representative TEM images of nanobulges manufactured without

aero-blading. The larger dark dots on a SiO₂ bead were observed for all nanobulges, which may be due to the thermal aggregation of singlet particles in the unshattered agglomerates during aero-sintering. This represents the effectiveness of aero-blading for forming unalloyed bulges in a few nanometer range on SiO₂ nanobeads for strong binding and consecutive inactivation of the adjacent HCoV.

The resulting nanobulges were dispersed in deionized water and coated on the filter nonwoven with HCoV to examine their anticoronaviral activity and compared with those treated with similar-sized individual Zn, Ag, and Cu particles (Fig. S5). Figs. 3A and 3B show the virus titers (expressed as PFU per mL) upon HCoV-229E exposure to the nanobulges in an aqueous solution and estimated the antiviral efficiencies, respectively. Compared to SiO₂ nanobeads alone, the nanobulges and individual nanoparticles exhibited a significant decrease in virus titer despite the differences between the nanobulges or nanoparticles. The antiviral activities from the nanoparticle (Zn, Ag, and Cu) treatments may be due mainly to the reactive oxygen species (ROS) generated by viral exposure to the released metallic ions, which can impair the respiratory enzymes and obstruct the RNA function caused by the breakage of S-S bonds, ultimately facilitating the disassembly and antiproliferation of the viruses (Ermini and Voliani, 2021; Minoshima et al., 2016; Seidi et al., 2021). The nanobulge treatments imparted comparable antiviral activities to the nanoparticles despite the significantly lower metallic content (<15 % in mass). The similar performance between Ag (or Cu) and Fe–Ag (or Fe–Cu) may be due to greater release

($r_{\text{release}} = \frac{c_p V_p}{m_s SSA t_{\text{exp}}}$, where c_p , V_p , m_s , SSA , and t_{exp} are the particle concentration, sample mass, specific surface area, and exposure time, respectively) of Ag (or Cu) ions from the fully Ag (or Cu) nanoparticle configuration (Park et al., 2020). This may be due to hydroxyl radicals that damage the viruses further as a coupled antiviral effect from the Fenton reaction catalyzed by the Fe ions released (Jones, 2007; Kim et al., 2019; Weiss et al., 2020), because hydroxyl radicals can be formed by the Fenton reaction under neutral pH conditions (Liu et al., 2021c). The Fenton-like reaction catalyzed by coexisting Zn, Ag, or Cu particles (Alkawareek et al., 2019; Goli, 2020; Grass et al., 2011) also affected the antiviral activities that may induce a greater difference between Fe–Zn nanobulges and Zn nanoparticles than that between Fe–Ag and Ag. This tendency was also observed after treating the HCoV-OC43 with nanobulges (Figs. S6A and S6B), confirming the influence of the Fenton-like reaction. Furthermore, the viral membrane (CoV_M) was first impaired upon the treatments, which was examined from quantification of the spike (CoV_S) and CoV_M gene expression of HCoV-229E by qRT-PCR (Fig. S6B). This suggests that the nanoparticles were first reacted with the CoV_M and subsequently bound to the CoV_S of the viruses to inactivate them (Jazie et al., 2021). For anticoronaviral test for the nanobulge coated air filter, a nanobulge (Fe–Zn; the efficiency positioned in the middle of the three nanobulges for the aqueous treatment) achieved a deposition intensity of $6.3 \times 10^{-5} \text{ g cm}^{-2}$ within 3 min while HCoV-229E was selected for the treatment with the filter because of its lower antiviral efficiencies in the case of an aqueous treatment (Fig. 3A

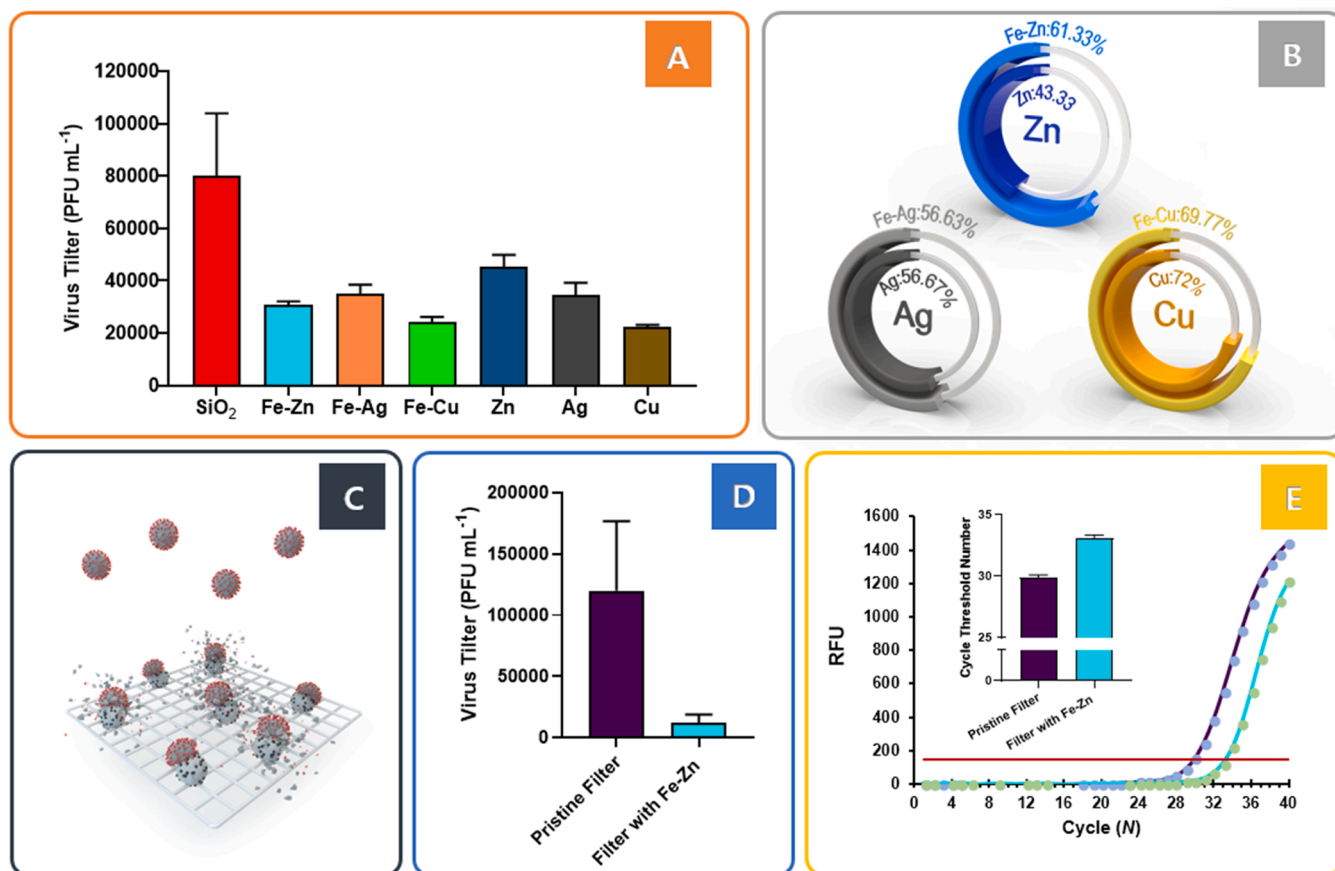


Fig. 3. Anticoronaviral activity of the resulting nanobulges, including similar-sized Zn, Ag, and Cu particles in an aqueous and air environment. (A) HCoV-229E virus titer upon aqueous treatments with the three nanobulges and nanoparticles for 15 min, including SiO₂ alone as the control. (B) Estimated efficiencies for comparing the anticoronaviral activity of Fe–Zn (or Fe–Ag, Fe–Cu) and Zn (or Ag, Cu). (C) Schematic diagram of the collection of aerosolized HCoV-229E on nanobulge-coated filter to examine the airborne anticoronaviral treatment. (D) Comparison of the HCoV-229E virus titer (based on the background subtraction of viable airborne viruses) upon 15 min exposure to the pristine and Fe–Zn nanobulge coated filters. (E) RFU profiles of the harvested viruses from the pristine and Fe–Zn nanobulge coated filters as a function of the cycle number. The inset graph shows the corresponding threshold numbers for the two filters to estimate anti-infectivity of the nanobulge coating.

vs. Fig. S6) as well as its greater stability to antiviral agents than the OC43 strain in a previous report (Hasan et al., 2020). In addition, the viral filtration efficiency of the Fe–Zn nanobulge coated filter in a single-pass air flow was comparable to that of the pristine filter, while no significant increases were observed in the pressure drop (i.e., representing air permeability) after the nanobulge coating (Fig. S7), supporting the adequacy of the nanobulge deposition intensity. Furthermore, the filtration efficiencies before and after co-loading of the nanobulges (3 min per day) and dust ($\sim 30 \mu\text{g m}^{-3}$ concentration) for 30 days were compared with pristine filter (Fig. S7). There were no significant differences between the pristine and nanobulge coated filters, suggesting that the periodical nanobulge coating to regenerate anti-coronaviral activity may not affect the original filtration performance of the filters. As shown in Fig. 3C, the aerosolized HCoV-229E strains were collected on Fe–Zn nanobulge coated filters (also on pristine filters for comparison), incubated for 15 min, and harvested for the plaque and qRT-PCR (observing the cycle threshold numbers (N) for a drastic increase in relative fluorescence units (RFU)) assays. The virus titer decreased by approximately 90 % (Fig. 3D) while anti-infectivity (AI) was also estimated to be approximately 90 % (Fig. 3E; $AI = (1 - \frac{1}{2^{N_p - N_{nc}}}) \times 100(\%)$, where N_p and N_{nc} are the cycle threshold numbers (inset in Fig. 3E) obtained from exposures to the pristine and nanobulge coated filters, respectively) in the presence of the nanobulges. These results suggest that the coexistence of the nanobulges and viruses on the filter surfaces for 15 min result in a significant loss of viral viability (ca. 90 % from 15 min coexistence; >99.9 % loss from 1 h coexistence, not shown in Figs. 3D and 3E). This was greater than that from aqueous exposure (Figs. 3A and 3B) due likely to the lower stability of viruses in air than that in an aqueous solution (Bhardwaj and Agrawal, 2020; Bormashenko et al., 2021; Sharma et al., 2021).

Representative AFM and SEM images (in the presence of a sputter coating, unlike nanobulge alone according to previous reports) (Caldas et al., 2020; Mondeja et al., 2021) revealed the attachment of the HCoV to the nanobulge surface in aqueous (Fig. 4A) and aerosol (Fig. 4B) state, respectively. These contacts are likely due to electrostatic interactions (negative surface charge of the nanobulges) (Adamczyk et al., 2021; Donskyi et al., 2021; Ye et al., 2015). In addition, physical engagement (nanoroughness by the Fe and Zn (or Ag, Cu) singlet particle decoration) (Nie et al., 2020) may provide channels for the transport of metallic ions to the viral surface and intraviral region for ROS generation (by Zn, Ag, or Cu ions) as well as hydroxyl radicals from the Fenton-mediated (catalyzed by Fe ions) and Fenton-like (catalyzed by Zn, Ag, or Cu ions) reaction that induced the coupled anticoronaviral activity (Fig. 4C).

The suppressing activity of the nanobulges on HCoV replication was

examined further by infecting WI-38 cells with HCoV-229E and different multiplicity of infection (MOI) with and without nanobulges, including the individual Zn, Ag, and Cu nanoparticles (Fig. S8). Although viral growth was proportional to the MOI, the nanobulge and nanoparticle exposures reduced viral growth significantly. Interestingly, the inhibition of the growth in human lung cells was more pronounced in the case of the nanobulge despite the lower metallic contents (<15 %) of the nanobulges. This suggests that the coupled activities of Fe and Zn (or Ag, Cu) induce the stronger cleavage of disulfide bonds of the spike protein (determining the infectivity of the virus) (Li et al., 2020), suppressing the significant increases in viral growth, even at the highest MOI compared to the individual metal nanoparticles. This highlights the effectiveness of the bimetallic composition and the bulge structure compared to conventional antiviral nanoparticles in anti-infectivity, particularly at > 1 MOI levels.

Regarding the *in vitro* cytotoxicity assessment of the nanobulges, HDF was selected as a representative of skin which is the first line of defense against foreign agents (Lujan and Sayes, 2017) while WI-38 was chosen as a model for inhalation exposure (Ianni et al., 2021). MTT assay was used to determine the viability of the cells treated with Fe–Zn, Fe–Ag, or Fe–Cu ($1\text{--}200 \mu\text{g mL}^{-1}$) for 24 h and 48 h. As shown in Fig. 5, the viabilities of both cell lines were dependent on the nanobulge concentration (and exposure time) due likely to the greater (and longer) release of metallic ions and contact with the bulges, which may lead to higher cellular toxicity from ROS generation, including a reduction of the mitochondrial function, micronuclei formation by induced apoptotic genes, chromosome abnormality, and DNA impairment (Botha et al., 2019; Chugh et al., 2018). The HDF cells exhibited slightly higher viability (>85 % after 48 h exposure at $200 \mu\text{g mL}^{-1}$) than the WI-38 cells (>83 %), whereas the lowest values were observed in both cell lines after Fe–Cu exposure for 48 h because of the greater activity of Cu in ROS generation than other individual particles (Matos et al., 2012; Park et al., 2019b). On the other hand, the lowest viabilities were greater than 80 %, even at $200 \mu\text{g mL}^{-1}$, which are in the acceptable range for cytocompatibility (ISO, 10993-5; 2009).

Although there were no significant alterations in the viability, the probability of oxidative damage to cellular molecules, such as nuclear DNA, resulted from the excessive ROS-induced senescent process (but not cell-killing) (Henson et al., 2019; Liguori et al., 2018; Nita and Grzybowski, 2016) was further determined. The ROS receptive dye, DCFH-DA, was used to examine oxidative stress and intracellular ROS. Compared to untreated cells, the order of ROS production after exposure to the nanobulges was Fe–Cu > Fe–Ag > Fe–Zn for both cell lines (1.53–2.37 for HDF; 1.55–2.81 for WI-38), as shown in Fig. S9A. These levels were significantly lower than those in a previous report in which ROS generation of more than eight times that of the control has only

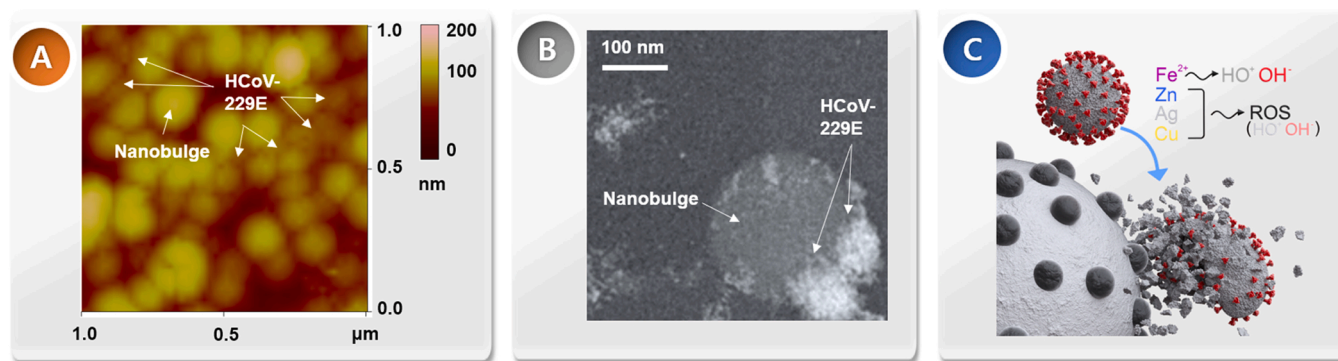


Fig. 4. Representative AFM and SEM images to identify the viral attachment to the Fe–Zn nanobulges. (A) AFM topograph containing HCoV-229E viruses and Fe–Zn nanobulges. The viral particles were observed at the inter-nanobulge spaces, presenting the contacts between the nanobulges and viruses. (B) SEM image of the nanobulge-coated filter after the virus collection. The contact between the nanobulge and the virus was also observed. (C) Illustration of contact between the nanobulge and virus for deriving the ROS generation triggered by the released metal ions and hydroxyl radical production from the Fenton-mediated and -like reactions.

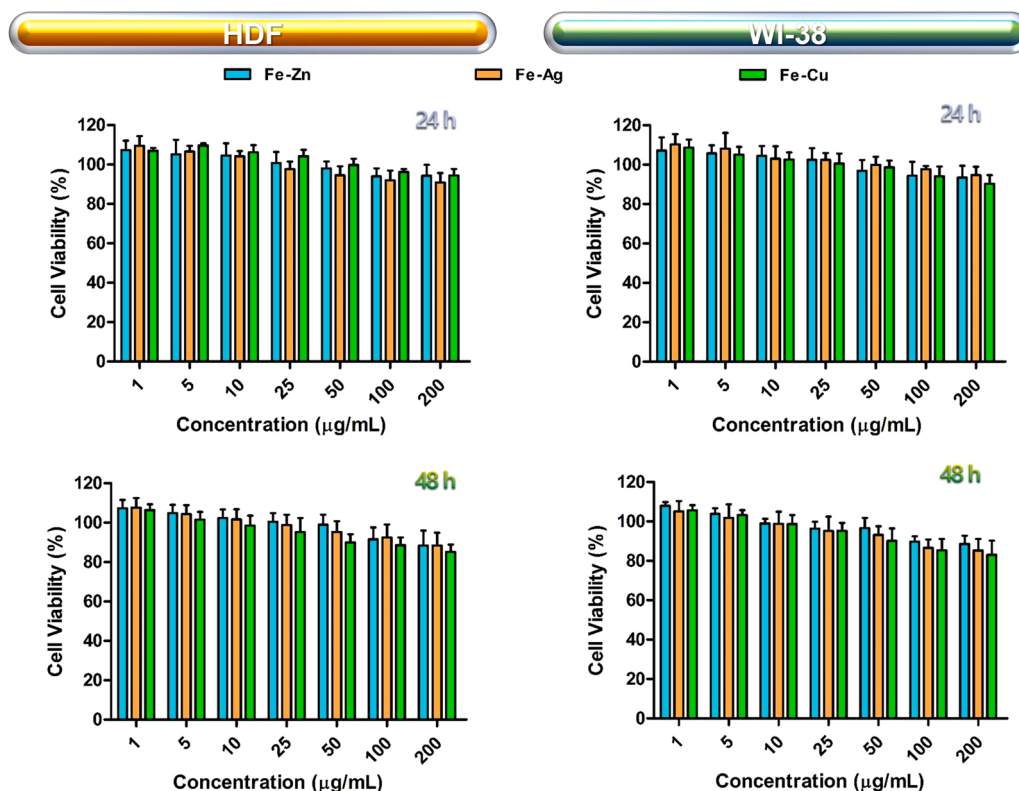


Fig. 5. In vitro cytotoxicity profiles of the resulting nanobulges in HDF and WI-38 cells. Using a MTT assay, the viabilities of the treated cells with different concentrations ($1\text{--}200\text{ }\mu\text{g mL}^{-1}$) were estimated after 24 h and 48 h incubation.

resulted in senescence (did not induce any significant morphological alterations) with increasing volume with large flat structures because of the small-spindle fusiform (Gautam et al., 2019). Furthermore, the profiles of cytotoxicity and ROS generation were observed in the order of Fe-Cu > Fe-Ag > Fe-Zn, showing that the cytotoxicity is related significantly to ROS production. Overall, the nanobulge exposure to HDF and WI-38 cells also produced ROS, whereas it can cause limited cytotoxicity unlike that in the viral exposure, supporting the selective inactivating activity because of the bimetallic bulge configuration.

Viability profiles (Fig. 6A) from the nanobulge (Fe-Zn, Fe-Ag, and Fe-Cu) exposures to HCoV-229E-infected MRC-5 cells reflected the order of the antiviral activity (Fe-Cu > Fe-Ag > Fe-Zn), indicating the antiviral-cell saving cotreatment of the nanobulges. Optical microscopy images (Fig. S9B) exhibited that cytoplasmic shrinkage, loss of cell-to-

cell contact, and reduced cell numbers were shown in the untreated cells (i.e., HCoV-229E-infected MRC-5 cells), unlike the cells treated with nanobulges. As shown in Fig. 6B, caspase-3 (an enzyme that induces apoptosis) activity (%) of the infected MRC-5 cells in the absence and presence of nanobulge treatment showed significant differences in the activity at both the different timepoints, supporting further the cotreatment of the nanobulges. To analyze the loss of genomic integrity and modulation of viral enzymes, the common markers related to apoptosis, ROS/reactive nitrogen species (RNS), and biogenesis (Fig. S9C) were targeted to examine the infectious activity of HCoV-229E in the absence and presence of the nanobulge treatment. The results demonstrated further effective suppression of the nanobulges on the infection-induced apoptosis in the host cells through ROS/RNS and the relevant transcription factors (Hang et al., 2015; Lara et al., 2010; Patoo

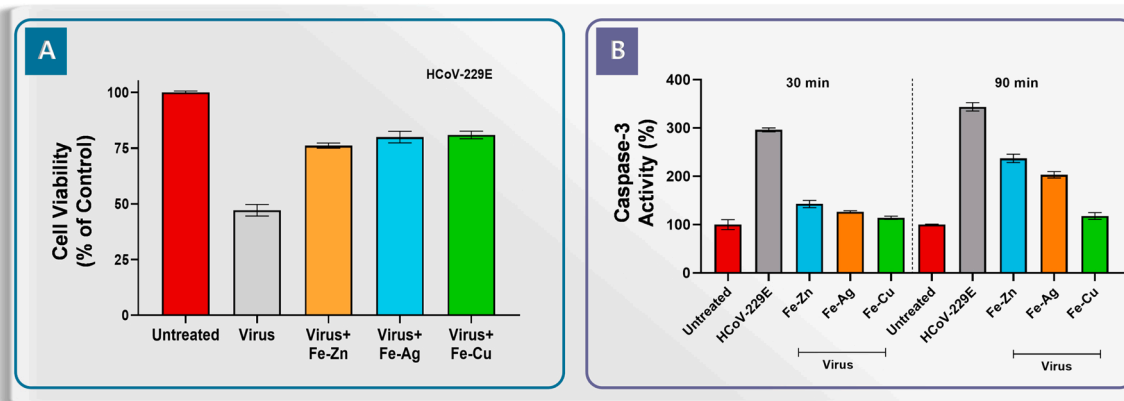


Fig. 6. Effects of the nanobulge exposure on viability and caspase-3 activity of HCoV-229E infected MRC-5 cells. (A) Viability profiles from anticoronaviral activity of the resulting nanobulges in an aqueous medium on the growth of HCoV-229E infection of MRC-5 cells by MTT assay. (B) Inhibition of caspase-3 activity of the infected MRC cells upon exposure to the nanobulges.

et al., 2022; Ramezani et al., 2018; Tavakoli and Hashemzadeh, 2020; Warnes et al., 2015).

The hemocompatibility of the nanobulges was examined by obtaining the degree of RBC destruction using the hemoglobin content (%) compared to the positive control, resulting in hemolysis after the incorporation of nanobulges with blood. The hemolysis percentage after incubation with nanobulges ($50\text{--}400\text{ }\mu\text{g mL}^{-1}$) in PBS was estimated. As shown in Fig. 7A, the hemolysis effects of the nanobulges showed concentration-dependent behavior. The hemolysis values at the highest concentration ($400\text{ }\mu\text{g mL}^{-1}$) were approximately 6.4 %, 6.7 %, and 7.3 % for Fe–Zn, Fe–Ag, and Fe–Cu, respectively, whereas PBS resulted in 3.6 % hemolysis. The order of hemolysis and the limited levels of RBC destruction of the nanobulges also coincided with the cytotoxicity and ROS generation, warranting further investigation using an *in vivo* model.

The *in vivo* biosafety was assessed by measuring the body weight, and the survival rate of the treated mice was monitored after the single-dose administration of nanobulges at 100 mg kg^{-1} . No abnormal alterations in the body weight (Fig. 7B) or changes in survival rate (Fig. 7C) of the treated mice were observed compared to the untreated group, showing the nanobulges have no fatal toxicity in the *in vivo* model. A histopathological-histomorphometric examination of the vital organs and blood biochemistry of the treated mice were conducted after 18 days of administration to ensure biosafety. The absence of abnormal histopathological findings (Fig. 7D and Table S2) supported the non-toxicity of the nanobulges. The following hematological parameters were analyzed from the blood samples of untreated and nanobulge treated mice to screen the biochemical parameters from the blood (Fig. S10; WBC, neutrophils; LYM, lymphocytes; MONO, monocytes; EOS, eosinophils; BASO, basophils; RBC; HGB; HCT; MCV; MCH,

mean corpuscular hemoglobin; MCHC, mean corpuscular hemoglobin concentration; RDW, red cell distribution width; PLT, platelets; MPV, mean platelet volume; ALP-PS, alkaline phosphatase; GOT-PS, AST; GPT-PS, alanine aminotransferase (ALT); BUN-PS, blood urea nitrogen; and CRE-PS, creatinine). All the tested parameters were in the normal range even for the treated mice compared to the untreated mice. The hepatotoxicity and nephrotoxicity were identified as the levels of the respective ALT/AST and BUN/CRE for the treated and untreated mice. No significant differences were observed between the mice groups (displaying in the normal range for all the biochemical parameters from the serum). The *in vitro* and *in vivo* experiments, including the blood chemistry of the nanobulges, showed that combining the developed electrically operable dispenser with air filters might be a good platform for reducing the airborne infection of the coronaviruses indoors.

The reconfigurable ability of the electrically operable dispenser was validated further by constructing the different nanobulges even without plasma ablation and aero-blading for simplifying the manufacture. Suprastructuring of the 15 nm SiO_2 bead (s- SiO_2) was attempted by vibrating the spray of the SiO_2 suspension containing an antiviral polymer (polyethyleneimine (PEI) or chitosan) (Mouritz et al., 2021) and passed through the electrically heated tube to thermodynamically construct bunches of s- SiO_2 beads and deposit the polymeric component on the beads. Representative TEM images (Fig. S11) revealed roughened antiviral surfaces of the resulting supraparticles (40–65 % antiviral efficiencies by modulating the PEI (or chitosan) contents for 15 min aqueous exposure) constructed through spherical agglomeration of the beads, warranting modular property of the manufacture to a variety of antiviral coatings for air filtration applications. Fig. S12 shows an electrically operable prototype for aero-manufacture of anticoronaviral

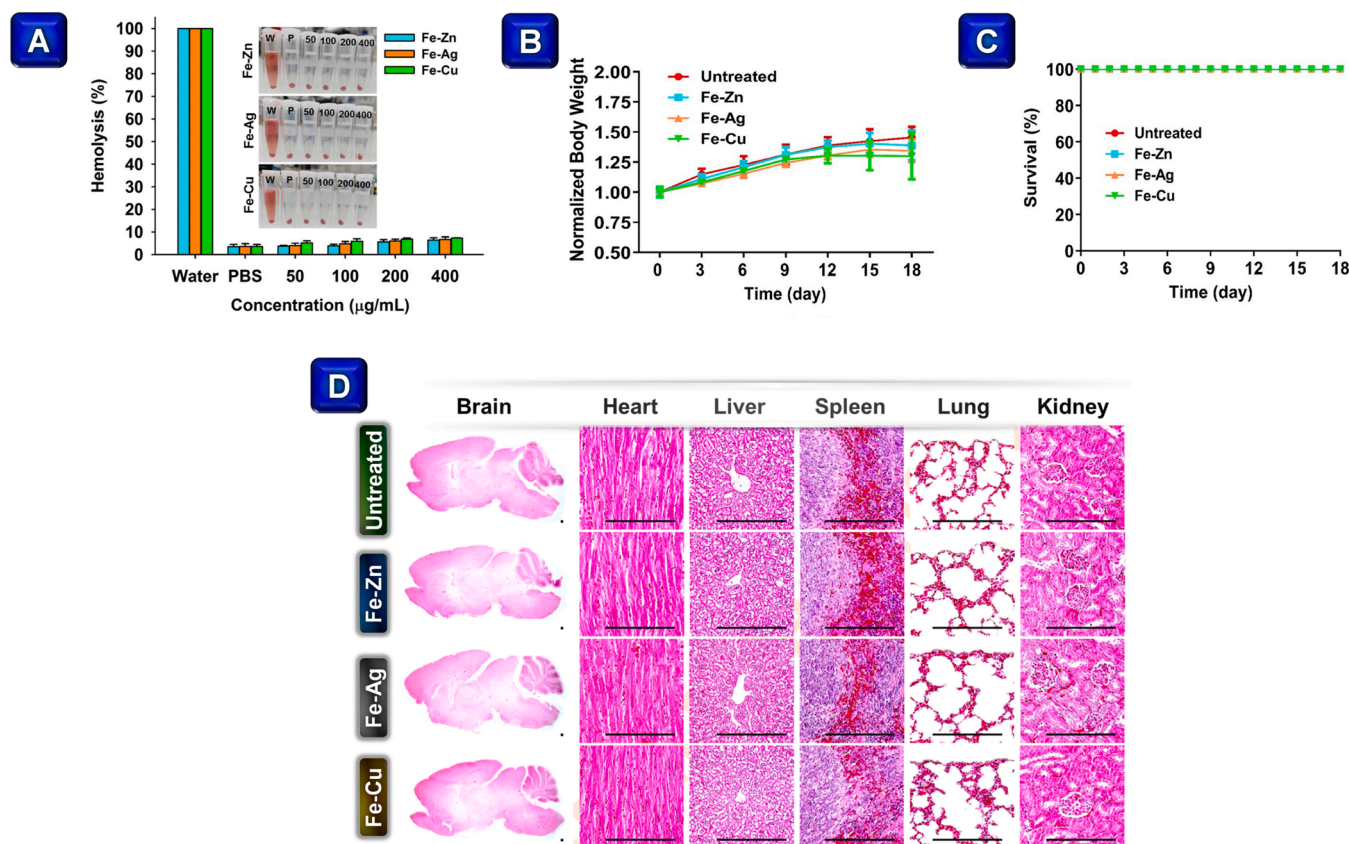


Fig. 7. Assay results to assess the hemotoxicity and *in vivo* systemic adverse effects of the nanobulge treatments. (A) Percentage hemolysis of RBCs treated with different concentrations of the resulting nanobulges ($50\text{--}400\text{ }\mu\text{g mL}^{-1}$). The inset shows relevant digital images from the treatments, and the letters W and P denoted the RBCs in water and PBS, respectively. (B) Monitored body weights (every three days), (C) Survival rates (every day), and (D) Histopathological profiles of the major organs from the untreated and nanobulge treated mice after 18 days. The mice were injected intraperitoneally with a single dose of 100 mg kg^{-1} on day 0. Scale bars, 480 μm .

face masks as a practical application, where representative low- and high-magnification SEM images demonstrated the coatings of nanobulges from an in-line production manner. The approach developed in this study may provide reconfigurable properties for various applications to suppress airborne infection and biological contamination of surfaces.

4. Conclusions

An aero-manufacture was used for the in-place supply of bimetallic nanobulges to provide an antiviral function on air filter surfaces during operation or abrogation after use to achieve electrically operable process, affordability, and biosafety of antiviral coatings. Fe-containing bimetallic (Fe–Zn, Fe–Ag, or Fe–Cu) agglomerates (consisting of <5 nm ultrafine particles) and SiO₂ nanobeads (ca. 130 nm) were coinjected into an orifice for cohesion and the aero-blading of agglomerates as singlet particles on beads. They were then passed through a heated tube to sinter the singlet particles on the beads, resulting in the formation of Fe–Zn, Fe–Ag, or Fe–Cu nanobulges for effective interactions with HCoV spikes. Unlike the dip coating of filter materials in an organic or inorganic antiviral suspension, the resulting aerosol nanobulges could be deposited directly on the filter surfaces by simple mechanical filtration (as just a 3 min antiviral coating) without generating aqueous or solid wastes. Hence, no additional unit operations and facilities were required to functionalize the antiviral filtering surfaces. A similar or superior antiviral performance between the resulting nanobulges (>55 % inactivation of the viruses for 15 min exposure in aqueous solutions; >99.0 % for 1 h exposure), and similar-sized individual Zn (43.4 %), Ag (56.7 %), and Cu (72.0 %) particles was obtained despite the significantly smaller fraction of metallic component (<15 %). The comparable antiviral activity to the individual particles was probably due to the cogeneration of reactive oxygen species and Fenton-mediated hydroxyl radicals from viral exposures to Zn, Ag, or Cu and Fe, respectively, upon engagement between the bimetallic bulges and coronaviral spikes. In the case of viral exposure to Fe–Zn nanobulges, the level of viral inactivation in both plaque and qRT-PCR assays was approximately 90 % for 15 min exposure, supporting the efficacy of the 3 min Fe–Zn coating. Decorating the significantly larger SiO₂ beads (being similar in size to the largest HCoV) with ultrafine bimetallic particles did not induce significant loss of the viability of mammalian cells and tissues. Two more concepts for constructing nanobulges were tested by reconfiguring the SiO₂ spraying conditions to modulate the developed platform. The in-flight manufacture for the direct dry deposition of bimetallic nanobulges on air filter surfaces provide a comparable antiviral function to traditional antiviral inorganic nanoparticles while retaining biosafety. In addition, the process is also suitable as an electrically operable dispenser capable of in-place antiviral coatings for biosafe air filtration and the modification of used filters during a viral infection pandemic despite the need of further assessment for bench-to-bedside translation. A significantly lower price of SiO₂ nanobeads (main component of the nanobulges) than pure metal nanoparticles (Zn, Ag, or Cu) and reconfigurable properties of the aero-manufacture to manipulate the configuration may also offer cost reduction for the realization of an in-place antiviral on air filters.

Environmental implication

This study developed a compact system of in-flight nanobulge manufacture to confer antiviral functions in-place on the filter surfaces by simply turning on a system to inactivate coronaviruses collected on the surfaces rapidly while retaining biosafety, thereby increasing the effectiveness of the air filtration in preventing the transmission of coronaviruses.

Coronavirus disease (COVID-19) is still ongoing despite the vaccination of a considerable number of people worldwide. The filtration of indoor air has been proven to be an effective intervention to suppress the

spread of COVID-19 because humans spend approximately 90% of their time indoors. The deposition of the contagious viruses on air filter surfaces has led to the adoption of antiviral coatings to reduce the spread of viral infections from this type of fomite. This has further caused issues regarding the deterioration of the antiviral performance during filter operation as well as nano- and bio-hazard (from the release of toxic metallic ions or viable viruses) from the discarded filters. The development of a plug-in safe-by-design antiviral coating is required to regenerate antiviral functions periodically and inactivate the infectiousness conveniently of the viruses collected before discarding the used filters. Although installing ultraviolet radiation devices near the filter unit was proposed as a rapidly implementable alternative to suppressing this fomite-mediated transmission, there are problems of limited radiation coverage for deep bed and cartridge filters as well as the photodegradation of filter materials. Another issue faced when applying exothermic material coatings on filters includes the need for temperature control, flame retardancy, and biosafety. To resolve these difficulties, this study developed a compact system of in-flight nanobulge manufacture to confer antiviral functions in-place on the filter surfaces by simply plugging in a system to inactivate coronaviruses collected on the surfaces rapidly while retaining biosafety, thereby increasing the effectiveness of the air filtration in preventing the transmission of coronaviruses. A single-pass aero-blading and -sintering Fe containing ultrafine particles (<5 nm) on SiO₂ nanobeads (ca. 130 nm) enabled the formation of surface roughness for their effective interaction with coronavirus spikes to generate reactive oxygen species and Fenton-mediated hydroxyl radicals, resulting in comparable antiviral activity to similar-sized individual Zn, Ag, or Cu particles despite the significantly smaller fraction of the metallic component.

CRediT authorship contribution statement

Jisoo Choi: Experiment, Anticoronaviral test, Writing – original draft. **Kishwor Poudel:** Experiment, Biosafety test, Writing – original draft. **Kang Sik Nam:** Experiment, Nanobulge manufacture, Writing – original draft. **Amin Piri:** Experiment, Anticoronaviral validation. **Adriana Rivera-Piza:** Experiment, Anticoronaviral mechanism. **Sae Kwang Ku:** Experiment, *In vivo* validation. **Jungho Hwang:** Conceptualization, Analysis, Writing – review & editing, Supervision, Funding acquisition. **Jong Oh Kim:** Conceptualization, Analysis, Writing – review & editing, Supervision. **Jeong Hoon Byeon:** Conceptualization, Investigation, Analysis, Writing – original draft, Writing – review & editing, Data curation, Supervision, Funding acquisition.

Declaration of Competing Interest

The authors declare that they have no known competing financial interests or personal relationships that could have appeared to influence the work reported in this paper.

Data availability

The authors do not have permission to share data.

Acknowledgments

This work was supported by the Technology Innovation Program (20007027, Mutually beneficial cooperative air purifying automobiles against atmospheric fine particles) funded By the Ministry of Trade, Industry & Energy (MOTIE, Korea). This work was also supported by Korea Environment Industry & Technology Institute (KEITI) through Core Technology Development Project for Environmental Diseases Prevention and Management, funded by Korea Ministry of Environment (MOE) (ARQ202201527001).

Appendix A. Supporting information

Supplementary data associated with this article can be found in the online version at [doi:10.1016/j.jhazmat.2022.130458](https://doi.org/10.1016/j.jhazmat.2022.130458).

References

- Adamczyk, Z., Batys, P., Barbasz, J., 2021. SARS-CoV-2 virion physicochemical characteristics pertinent to abiotic substrate attachment. *Curr. Opin. Colloid Interface Sci.* 55, 101466. <https://doi.org/10.1016/j.cocis.2021.101466>.
- Agarwal, N., Meena, C.S., Raj, B.P., Saini, L., Kumar, A., Gopalakrishnan, N., Kumar, A., Balam, N.B., Alam, T., Kapoor, N.R., Aggarwal, V., 2021. Indoor air quality improvement in COVID-19 pandemic: review. *Sustain. Cities Soc.* 70, 102942. <https://doi.org/10.1016/j.scs.2021.102942>.
- Alkawareek, M.Y., Bahloul, A., Abulatefeh, S.R., Alkily, A.M., 2019. Synergistic antibacterial activity of silver nanoparticles and hydrogen peroxide. *PLOS One* 14, e0220575. <https://doi.org/10.1371/journal.pone.0220575>.
- Annajvala, M.K., Mohri, H., Wang, P., Nair, M., Zucker, J.E., Sheng, Z., Gomez-Simmonds, A., Kelley, A.L., Tagliavia, M., Huang, Y., Bedford, T., Ho, D.D., Uhlemann, A.-C., 2021. Emergence and expansion of SARS-CoV-2 B.1.526 after identification in New York. *Nature* 597, 703–708. <https://doi.org/10.1038/s41586-021-03908-2>.
- Balagna, C., Francese, R., Perero, S., Lembo, D., Ferraris, M., 2021. Nanostructured composite coating endowed with antiviral activity against human respiratory viruses deposited on fibre-based air filters. *Surf. Coat. Technol.* 409, 126873. <https://doi.org/10.1016/j.surfcoat.2021.126873>.
- Barciszewska, A.-M., 2021. Elucidating oxidative distress in COVID-19 and methods of its prevention. *Chem. Biol. Interact.* 344, 109501. <https://doi.org/10.1016/j.cbi.2021.109501>.
- Bazzazpour, S., Rahmatinia, M., Mohebbi, S.R., Hadei, M., Shahsavani, A., Hopke, P.K., Houshmand, B., Raiesi, A., Jafari, A.J., Yarahmadi, M., Farhadi, M., Hasanazadeh, V., Kermani, M., Vaziri, M.H., Tanhaei, M., Zali, M.R., Alipour, M.R., 2021. The detection of SARS-CoV-2 RNA in indoor air of dental clinics during the COVID-19 pandemic. *Environ. Sci. Pollut. Res.* <https://doi.org/10.1007/s11356-021-15607-6>. <https://doi.org/10.1007/s11356-021-15607-6>.
- Bhardwaj, R., Agrawal, A., 2020. How coronavirus survives for days on surfaces. *Phys. Fluids* 32, 111706. <https://doi.org/10.1063/5.0033306>.
- Bormashenko, E., Fedorets, A.A., Dombrovsky, L.A., Nosonovsky, M., 2021. Survival of virus particles in water droplets: hydrophobic forces and Landauer's principle. *Entropy* 23, 181. <https://doi.org/10.3390/e23020181>.
- Botha, L., Elemike, E.E., Horn, S., Onwudike, D.C., Giesy, J.P., Wepener, V., 2019. Cytotoxicity of Ag, Au and Ag-Au bimetallic nanoparticles prepared using golden rod (*Solidago canadensis*) plant extract. *Sci. Rep.* 9, 4169. <https://doi.org/10.1038/s41598-019-40816-y>.
- Byeon, J.H., Kim, J.-W., 2010. Production of carbonaceous nanostructures from a silver-carbon ambient spark. *Appl. Phys. Lett.* 96, 153102. <https://doi.org/10.1063/1.3396188>.
- Byeon, J.H., Roberts, J.T., 2012. Aerosol based fabrication of thiol-capped gold nanoparticles and their application for gene transfection. *Chem. Mater.* 24, 3544–3549. <https://doi.org/10.1021/cm300601m>.
- Caldas, T.L., Carneiro, F.A., Higa, L.M., Monteiro, F.L., da Silva, G.P., da Costa, L.J., Durigon, E.L., Tanuri, A., de Souza, W., 2020. Ultrastructural analysis of SARS-CoV-2 interactions with the host cell via high resolution scanning electron microscopy. *Sci. Rep.* 10, 16099. <https://doi.org/10.1038/s41598-020-73162-5>.
- Cheng, K.L., 2006. The negative charge of nanoparticles. *Microchem. J.* 82, 119–120. <https://doi.org/10.1016/j.microc.2005.11.002>.
- Cheng, Y., Ma, N., Witt, C., Rapp, S., Wild, P.S., Andreae, M.O., Pöschl, U., Su, H., 2021. Face masks effectively limit the probability of SARS-CoV-2 transmission. *Science* 372, 1439–1443. <https://doi.org/10.1126/science.abg6296>.
- Christopherson, D.A., Yao, W.C., Lu, M., Vijayakumar, R., Sedaghat, A.R., 2020. High-efficiency particulate air filters in the era of COVID-19: function and efficacy. *Otolaryngol. Head. Neck Surg.* 163, 1153–1155. <https://doi.org/10.1177/0194599820941838>.
- Chugh, H., Sood, D., Chandra, I., Tomar, V., Dhawan, G., Chandra, R., 2018. Role of gold and silver nanoparticles in cancer nano-medicine. *Artif. Cells Nanomed. Biotechnol.* 46, 1210–1220. <https://doi.org/10.1080/21691401.2018.1449118>.
- Correia, G., Rodrigues, L., da Silva, M.G., Gonçalves, S.T., 2020. Airborne route and bad use of ventilation systems as non-negligible factors in SARS-CoV-2 transmission. *Med. Hypotheses* 141, 109781. <https://doi.org/10.1016/j.mehy.2020.109781>.
- Curtius, J., Granzin, M., Schrod, J., 2021. Testing mobile air purifier in a school classroom: reducing the airborne transmission risk for SARS-CoV-2. *Aerosol Sci. Technol.* 55, 586–599. <https://doi.org/10.1080/02786826.2021.1877257>.
- Das, M., Goswami, U., Ghosh, S.S., Chattopadhyay, A., 2018. Bimetallic Fe-Cu nanocomposites on sand particles for the inactivation of clinical isolates and point-of-use water filtration. *ACS Appl. Bio Mater.* 1, 2153–2166. <https://doi.org/10.1021/acsbm.8b00572>.
- Donskyi, I.S., Nie, C., Ludwig, K., Trimpert, J., Ahmed, R., Quaas, E., Achazi, K., Radnik, J., Adeli, M., Haag, R., Osterrieder, K., 2021. Graphene sheets with defined dual functionalities for the strong SARS-CoV-2 interactions. *Small* 17, 2007091. <https://doi.org/10.1002/sml.202007091>.
- Egan, C.K., Paesani, F., 2018. Assessing many-body effects of water self-ions. I: OH⁻(H₂O)_n clusters. *J. Chem. Theory Comput.* 14, 1982–1997. <https://doi.org/10.1021/acs.jctc.7b01273>.
- Elsaid, A.M., Ahmed, M.S., 2021. Indoor air quality strategies for air-conditioning and ventilation systems with the spread of the global coronavirus (COVID-19) epidemic: Improvements and recommendations. *Environ. Res.* 199, 111314. <https://doi.org/10.1016/j.envres.2021.111314>.
- Ermini, M.L., Voliani, V., 2021. Antimicrobial nano-agents: the copper age. *ACS Nano* 15, 6008–6029. <https://doi.org/10.1021/acsnano.0c10756>.
- Fan, X., Yang, F., Nie, C., Ma, L., Cheng, C., Haag, R., 2021. Biocatalytic nanomaterials: A new pathway for bacterial disinfection. *Adv. Mater.* 33, 2100637. <https://doi.org/10.1002/adma.202100637>.
- Feng, J., Biskos, G., Schmidt-Ott, A., 2015. Toward industrial scale synthesis of ultrapure singlet nanoparticles with controllable sizes in a continuous gas-phase process. *Sci. Rep.* 5, 15788. <https://doi.org/10.1038/srep15788>.
- Gautam, M., Park, D.H., Park, S.J., Nam, K.S., Park, G.Y., Hwang, J., Yong, C.S., Kim, J. O., Byeon, J.H., 2019. Plug-in safe-by-design nanoinorganic antibacterials. *ACS Nano* 13, 12798–12809. <https://doi.org/10.1021/acsnano.9b04939>.
- Goli, M., 2020. Review of novel human β -coronavirus (2019-nCoV or SARS-CoV-2) from the food industry perspective – appropriate approaches to food production technology. *Food Sci. Nutr.* 8, 5228–5237. <https://doi.org/10.1002/fsn3.1892>.
- Grass, G., Rensing, C., Solioz, M., 2011. Metallic copper as an antimicrobial surface. *Appl. Environ. Microbiol.* 77, 1541–1547. <https://doi.org/10.1128/AEM.02766-10>.
- Hadei, M., Mohebbi, S.R., Hopke, P.K., Shahsavani, A., Bazzazpour, S., Alipour, M., Jafari, A.J., Bandpey, A.M., Zali, A., Yarahmadi, M., Farhadi, M., Rahmatinia, M., Hasanazadeh, V., Zazari, S.S.H., Asadzadeh-Aghdaei, H., Tanhaei, M., Zali, M.R., Kermani, M., Vaziri, M.H., Chobineh, H., 2021. Presence of SARS-CoV-2 in the air of public places and transportation. *Atmos. Pollut. Res.* 12, 255–259. <https://doi.org/10.1016/j.apr.2020.12.016>.
- Häffner, S.M., Parra-Ortiz, E., Browning, K.L., Jørgensen, E., Skoda, M.W.A., Montis, C., Li, X., Berti, D., Zhao, D., Malmsten, M., 2021. Membrane interactions of virus-like mesoporous silica nanoparticles. *ACS Nano* 15, 6787–6800. <https://doi.org/10.1021/acsnano.0c10378>.
- Hang, X., Peng, H., Song, H., Qi, Z., Miao, X., Xu, W., 2015. Antiviral activity of cuprous oxide nanoparticles against hepatitis C virus *in vitro*. *J. Virol. Methods* 222, 150–157. <https://doi.org/10.1016/j.jviromet.2015.06.010>.
- Hasan, M.A., Esther, A.C.M., Dey, A., Yarahmadi, M., Farhadi, M., Rahmatinia, M., 2020. A review on coronavirus survivability on material's surfaces: present research scenarios, technologies and future directions. *Surf. Eng.* 36, 1226–1239. <https://doi.org/10.1080/02670844.2020.1833277>.
- Henson, T.E., Navratilova, J., Tennant, A.H., Bradham, K.D., Rogers, K.R., Hughes, M.F., 2019. *In vitro* intestinal toxicity of copper oxide nanoparticles in rat and human cell models. *Nanotoxicology* 13 (795–811), 2019. <https://doi.org/10.1080/17435390.2019.1578428>.
- Hodek, J., Zajíčková, V., Lovětinská-Šlamborová, I., Stibor, I., Müllerová, J., Weber, J., 2016. Protective hybrid coating containing silver, copper and zinc cations effective against human immunodeficiency virus and other enveloped viruses. *BMC Microbiol.* 16, 56. <https://doi.org/10.1186/s12866-016-0675-x>.
- Horváth, E., Rossi, L., Mercier, C., Lehmann, C., Sienkiewicz, A., Forró, L., 2020. Photocatalytic nanowire-based air filter: towards reusable protective masks. *Adv. Funct. Mater.* 30, 2004615. <https://doi.org/10.1002/adfm.202004615>.
- Huang, H., Fan, C., Li, M., Nie, H.-L., Wang, F.-B., Wang, H., Wang, R., Xia, J., Zheng, X., Zuo, X., Huang, J., 2020. COVID-19: a call for physical scientists and engineers. *ACS Nano* 14, 3747–3754. <https://doi.org/10.1021/acsnano.0c02618>.
- Ianni, E.D., Erdem, J.S., Möller, P., Sahlgren, N.M., Poulsen, S.S., Knudsen, K.B., Zienoldiny, S., Saber, A.T., Wallin, H., Vogel, U., Jacobsen, N.R., 2021. *In vitro-in vivo* correlations of pulmonary inflammation and genotoxicity of MWCNT. *Part. Fibre Toxicol.* 18, 25. <https://doi.org/10.1186/s12989-021-00413-2>.
- Imani, S.M., Ladouceur, L., Marshall, T., MacLachlan, R., Soleymani, L., Didar, T.F., 2020. Antimicrobial nanomaterials and coatings: current mechanisms and future perspectives to control the spread of viruses including SARS-CoV-2. *ACS Nano* 14, 12341–12369. <https://doi.org/10.1021/acsnano.0c05937>.
- ISO 10993-5: 2009, 2019. Biological evaluation of medical devices—Part 5: Tests for *in vitro* cytotoxicity. International Organization for Standardization Geneva.
- Javidpour, L., Božić, A., Naji, A., Podgornik, R., 2021. Electrostatic interactions between the SARS-CoV-2 virus and a charged electret fibre. *Soft Matter* 17, 4296–4303. <https://doi.org/10.1039/D1SM00232E>.
- Jazie, A.A., Albaaji, A.J., Abed, S.A., 2021. A review on recent trends of antiviral nanoparticles and airborne filters: special insight on COVID-19 virus. *Air Qual. Atmos. Health* 14, 1811–1824. <https://doi.org/10.1007/s11869-021-01055-1>.
- Joe, Y.H., Woo, K., Hwang, J., 2014. Fabrication of an anti-viral air filter with SiO₂-Ag nanoparticles and performance evaluation in a continuous airflow condition. *J. Hazard. Mater.* 280, 356–363. <https://doi.org/10.1016/j.jhazmat.2014.08.013>.
- Jones, S., 2007. Antibiotics and death – the Fenton connection. *Nat. Rev. Microbiol.* 5, 829. <https://doi.org/10.1038/nrmicro1783>.
- Jones, T.C., Biele, G., Mühlemann, B., Veith, T., Schneider, J., Beheim-Schwarzbach, J., Bleicker, T., Tesch, J., Schmidt, M.L., Sander, L.E., Kurth, F., Menzel, P., Schwarzer, R., Zuchowski, M., Hofmann, J., Krumbholz, A., Stein, A., Edelmann, A., Corman, V.M., Drosten, C., 2021. Estimating infectiousness throughout SARS-CoV-2 infection course. *Science* 373, eabi5273. <https://doi.org/10.1126/science.abi5273>.
- Kim, H.-E., Lee, H.-J., Kim, M.S., Kim, T., Lee, H., Kim, H.-H., Cho, M., Hong, S.-W., Lee, C., 2019. Differential microbicidal effects of bimetallic iron-copper nanoparticles on *Escherichia coli* and MS2 coliphage. *Environ. Sci. Technol.* 53, 2679–2687. <https://doi.org/10.1021/acs.est.8b06077>.
- Kwon, K.Y., Cheeseman, S., Frias-De-Diego, A., Hong, H., Yang, J., Jung, W., Yin, H., Murdoch, B.J., Scholle, F., Crook, N., Crisci, E., Dickey, M.D., Truong, V.K., Kim, T.-I., 2021. A liquid metal mediated metallic coating for antimicrobial and antiviral fabrics. *Adv. Mater.* 33, 2104298. <https://doi.org/10.1002/adma.202104298>.

- Lara, H.H., Ayala-Núñez, N.V., Ixtepan-Turrent, L., Rodríguez-Padilla, C., 2010. Mode of antiviral action of silver nanoparticles against HIV-1. *J. Nanobiotechnol.* 8, 1. <https://doi.org/10.1186/1477-3155-8-1>.
- Li, B., Wang, D., Lee, M.M.S., Wang, W., Tan, Q., Zhao, Z., Tang, B.Z., Huang, X., 2021. Fabrics attached with highly efficient aggregation-induced emission photosensitizer: toward self-antiviral personal protective equipment. *ACS Nano* 15, 13857–13870. <https://doi.org/10.1021/acsnano.1c06071>.
- Li, Q., Wu, J., Nie, J., Zhang, L., Hao, H., Liu, S., Zhao, C., Zhang, Q., Liu, H., Nie, L., Qin, H., Wang, M., Lu, Q., Li, X., Sun, Q., Liu, J., Zhang, L., Li, X., Huang, W., Wang, Y., 2020. The impact of mutations in SARS-CoV-2 spike on viral infectivity and antigenicity. *Cell* 182, 1284–1294. <https://doi.org/10.1016/j.cell.2020.07.012>.
- Liguori, I., Russo, G., Curcio, F., Bulli, G., Aran, L., Della-Morte, D., Gargiulo, G., Testa, G., Cacciatore, F., Bonaduce, D., Abete, P., 2018. Oxidative stress, aging, and diseases. *Clin. Interv. Aging* 13, 757–772. <https://doi.org/10.2147/CIA.S158513>.
- Liu, D.X., Liang, J.Q., Fung, T.S., 2021a. Human coronavirus-229E, -OC43, -NL63, and -HKU1 (*Coronaviridae*). *Encyclopedia of Virology* (Fourth Edition) 2, 428–440. <https://doi.org/10.1016/B978-0-12-809633-8.21501-X>.
- Liu, Y., Zhou, Q., Li, Z., Zhang, A., Zhan, J., Miruka, A.C., Gao, X., Wang, J., 2021c. Effectiveness of chelating agent-assisted Fenton-like processes on remediation of glucocorticoid-contaminated soil using chemical and biological assessment: performance comparison of CaO₂ and H₂O₂. *Environ. Sci. Pollut. Res.* 28, 310–320. <https://doi.org/10.1007/s11356-021-15150-4>.
- Liu, Z., Zhao, X., Yu, B., Zhao, N., Zhang, C., Xu, F.-J., 2021b. Rough carbon-iron oxide nanohybrids for near-infrared-II light-responsive synergistic antibacterial therapy. *ACS Nano* 15, 7482–7490. <https://doi.org/10.1021/acsnano.1c00894>.
- Lujan, H., Sayes, C.M., 2017. Cytotoxicological pathways induced after nanoparticle exposure: studies of oxidative stress at the 'nano-bio' interface. *Toxicol. Res.* 6, 580–594. <https://doi.org/10.1039/c7tx00119c>.
- Macfarlane, R.J., 2021. From nano to macro: Thinking bigger in nanoparticle assembly. *Nano Lett.* 21, 7432–7434. <https://doi.org/10.1021/acsnanolett.1c02724>.
- Malloy, J., Quintana, A., Jensen, C.J., Liu, K., 2021. Efficient and robust metallic nanowire foams for deep submicrometer particulate filtration. *Nano Lett.* 21, 2968–2974. <https://doi.org/10.1021/acsnanolett.1c00050>.
- Marková, Z., Šišková, K.M., Filip, J., Čuda, J., Kolář, M., Šafářová, K., Medřík, I., Zboril, R., 2013. Air stable magnetic bimetallic Fe–Ag nanoparticles for advanced antimicrobial treatment and phosphorus removal. *Environ. Sci. Technol.* 47, 5285–5293. <https://doi.org/10.1021/es304693g>.
- Matos, L., Gouveia, A., Almeida, H., 2012. Copper ability to induce premature senescence in human fibroblasts. *Age* 34, 783–794. <https://doi.org/10.1007/s11357-011-9276-7>.
- Minoshima, M., Lu, Y., Kimura, T., Nakano, R., Ishiguro, H., Kubota, Y., Hashimoto, K., Sunada, K., 2016. Comparison of the antiviral effect of solid-state copper and silver compounds. *J. Hazard. Mater.* 312, 1–7. <https://doi.org/10.1016/j.jhazmat.2016.03.023>.
- Mondeja, N., Valdes, O., Resik, S., Vizcaino, A., Acosta, E., Montalván, A., Paez, A., Mune, M., Rodríguez, R., Valdés, J., Gonzalez, G., Sanchez, D., Falcón, V., González, Y., Kourí, V., 2021. The IPK virology research group, A. Díaz, M. Guzmán, SARS-CoV-2: preliminary study of infected human nasopharyngeal tissue by high resolution microscopy. *Virology* 18, 149. <https://doi.org/10.1186/s12985-021-01620-1>.
- Mouchtouri, V.A., Koureas, M., Kyritsi, M., Vontas, A., Kourantis, L., Sapounas, S., Rigakos, G., Petinaki, E., Tsioltras, S., Hadjichristodoulou, C., 2020. Environmental contamination of SARS-CoV-2 on surfaces, air-conditioner and ventilation systems. *Int. J. Hyg. Environ. Health* 230, 113599. <https://doi.org/10.1016/j.ijheh.2020.113599>.
- Mouritz, A.P., Galos, J., Linklater, D.P., Ladani, R.B., Kandare, E., Crawford, R.J., Ivanova, E.P., 2021. Towards antiviral polymer composites to combat COVID-19 transmission. *Nano Sel.* 2, 2061–2071. <https://doi.org/10.1002/nano.202100078>.
- Mousavi, E.S., Kananizadeh, N., Martinello, R.A., Sherman, J.D., 2021. COVID-19 outbreak and hospital air quality: a systemic review of evidence on air filtration and recirculation. *Environ. Sci. Technol.* 55, 4134–4147. <https://doi.org/10.1021/acs.est.0c03247>.
- Nazarenko, Y., 2020. Air filtration and SARS-CoV-2. *Epidemiol. Health* 42, e2020049. <https://doi.org/10.4178/epih.e2020049>.
- Neal, C.J., Fox, C.R., Sakthivel, T.S., Kumar, U., Fu, Y., Drake, C., Parks, G.D., Seal, S., 2021. Metal-mediated nanoscale cerium oxide inactivates human coronavirus and rhinovirus by surface disruption. *ACS Nano* 15, 14544–14556. <https://doi.org/10.1021/acsnano.1c04142>.
- Nie, C., Stadtmüller, M., Yang, H., Xia, Y., Wolff, T., Cheng, C., Haag, R., 2020. Spiky nanostructures with geometry-matching topography for virus inhibition. *Nano Lett.* 20, 5367–5375. <https://doi.org/10.1021/acsnanolett.0c01723>.
- Nita, M., Grzybowski, A., 2016. The role of the reactive oxygen species and oxidative stress in the pathomechanism of the age-related ocular diseases and other pathologies of the anterior and posterior eye segments in adults. *Oxid. Med. Cell. Longev.* 2016, 3164734. <https://doi.org/10.1155/2016/3164734>.
- Novelli, F., Lopez, M.B., Schwaab, G., Cuenya, B.R., Havenith, M., 2019. Water solvation of charged and neutral gold nanoparticles. *J. Phys. Chem. B* 123, 6521–6528. <https://doi.org/10.1021/acs.jpcc.9b02358>.
- Orlando, R., Polat, M., Afshari, A., Johnson, M.S., Fojan, P., 2021. Electrospun nanofibre air filters for particles and gaseous pollutants. *Sustainability* 13, 6553. <https://doi.org/10.3390/su13126553>.
- Pal, A., Squitti, R., Picozza, M., Pawar, A., Rongioletti, M., Dutta, A.K., Sahoo, S., Goswami, K., Sharma, P., Prasad, R., 2021. Zinc and COVID-19: basis of current clinical trials. *Biol. Trace Elem. Res.* 199, 2882–2892. <https://doi.org/10.1007/s12011-020-02437-9>.
- Park, D.H., Joe, Y.H., Hwang, J., 2019a. Dry aerosol coating of anti-viral particles on commercial air filters using a high-volume flow atomizer. *Aerosol Air Qual. Res.* 19, 1636–1644. <https://doi.org/10.4209/aaqr.2019.04.0212>.
- Park, D.H., Gautam, M., Park, S.J., Hwang, J., Yong, C.S., Kim, J.O., Byeon, J.H., 2019b. Plug-and-play safe-by-design production of metal-doped tellurium nanoparticles with safer antimicrobial activities. *Environ. Sci. Nano* 6, 2074–2083. <https://doi.org/10.1039/C9EN00372J>.
- Park, D.H., Joe, Y.H., Hwang, J., Byeon, J.H., 2020. Evaporation-condensation in the presence of unipolar ionic flow for solvent-free production of ultrasmall antibacterial particles. *Chem. Eng. J.* 381, 122639. <https://doi.org/10.1016/j.cej.2019.122639>.
- Park, D.H., Choi, J., Piri, A., Hwang, J., Byeon, J.H., 2021a. Nano-dry-salt deposition on electret nonwoven confers anticoronaviral effect while retaining aerosol filtration performance. *Environ. Sci. Nano* 8, 2780–2791. <https://doi.org/10.1039/D1EN00369K>.
- Park, K., Kang, S., Park, J.-W., Hwang, J., 2021b. Fabrication of silver nanowire coated fibrous air filter medium via a two-step process of electrospinning and electrospray for anti-bioaerosol treatment. *J. Hazard. Mater.* 411, 125043. <https://doi.org/10.1016/j.jhazmat.2021.125043>.
- Patro, T.S., Khanday, F., Qurashi, A., 2022. Prospectus of advanced nanomaterials for antiviral properties. *Mater. Adv.* 3, 2960–2970. <https://doi.org/10.1039/D1MA00541C>.
- Radney, J.G., Weaver, J.L., Vicenzi, E.P., Staymates, M.E., Zangmeister, C.D., 2021. Filter inserts impact cloth mask performance against nano- to micro-sized particles. *ACS Nano* 15, 12860–12868. <https://doi.org/10.1021/acsnano.1c05182>.
- Ramezani, A., Nahad, M.P., Faghiloo, E., 2018. The role of Nrf2 transcription factor in viral infection. *J. Cell. Biochem.* 119, 6366–6382. <https://doi.org/10.1002/jcb.26897>.
- Sathya, K., Saravanathamizhan, R., Baskar, G., 2018. Ultrasonic assisted green synthesis of Fe and Fe/Zn bimetallic nanoparticles for *in vitro* cytotoxicity study against HeLa cancer cell line. *Mol. Biol. Rep.* 45, 1397–1404. <https://doi.org/10.1007/s11033-018-4302-9>.
- Seidi, F., Deng, C., Zhong, Y., Liu, Y., Huang, Y., Li, C., Xiao, H., 2021. Functionalized masks: powerful materials against COVID-19 and future pandemics. *Small* 17, 2102453. <https://doi.org/10.1002/smll.202102453>.
- Sellaoui, L., Badawi, M., Monari, A., Tatarchuk, T., Jemli, S., Dotto, G.L., Bonilla-Petriciolet, A., Chen, Z., 2021. Make it clean, make it safe: A review on virus elimination via adsorption. *Chem. Eng. J.* 412, 128682. <https://doi.org/10.1016/j.cej.2021.128682>.
- Sharma, A., Preece, B., Swann, H., Fan, X., McKenney, R.J., Ori-McKenney, K.M., Saffarian, S., Vershinin, M.D., 2021. Structural stability of SARS-CoV-2 virus like particles degrades with temperature. *Biochem. Biophys. Res. Commun.* 534, 343–346. <https://doi.org/10.1016/j.bbrc.2020.11.080>.
- Shen, H., Zhou, Z., Wang, H., Zhang, M., Han, M., Durkin, D.P., Shuai, D., Shen, Y., 2021b. Development of electrospun nanofibrous filters for controlling coronavirus aerosols. *Environ. Sci. Technol. Lett.* 8, 545–550. <https://doi.org/10.1021/acs.estlett.1c00337>.
- Shen, J., Kong, M., Dong, B., Birnkrant, M.J., Zhang, J., 2021a. A systematic approach to estimating the effectiveness of multi-scale IAQ strategies for reducing the risk of airborne infection of SARS-CoV-2. *Build. Environ.* 200, 107926. <https://doi.org/10.1016/j.buildenv.2021.107926>.
- Siddiqui, R., Khamis, M., Ibrahim, T., Khan, N.A., 2020. SARS-CoV-2: disinfection strategies to prevent transmission of neuropathogens via air conditioning systems. *ACS Chem. Neurosci.* 11, 3177–3179. <https://doi.org/10.1021/acscchemneuro.0c00595>.
- Sleiti, A.K., Ahmed, S.F., Ghani, S.A., 2021. Spreading of SARS-CoV-2 via heating, ventilation, and air conditioning systems – an overview of energy perspective and potential solutions. *J. Energy Resour. Technol.* 143, 080803. <https://doi.org/10.1115/1.4048943>.
- Sodiq, A., Khan, M.A., Naas, M., Amhamed, A., 2021. Addressing COVID-19 contagion through the HVAC systems by reviewing indoor airborne nature of infectious microbes: will an innovative air recirculation concept provide a practical solution? *Environ. Res.* 199, 111329. <https://doi.org/10.1016/j.envres.2021.111329>.
- Stabryla, L.M., Johnson, K.A., Diemler, N.A., Cooper, V.S., Millstone, J.E., Haig, S.-J., Gilbertson, L.M., 2021. Role of bacterial motility in differential resistance mechanisms of silver nanoparticles and silver ions. *Nat. Nanotechnol.* 16, 996–1003. <https://doi.org/10.1038/s41565-021-00929-w>.
- Sunday, M.O., Sakugawa, H., 2020. A simple, inexpensive method for gas-phase singlet oxygen generation from sensitizer-impregnated filters: potential application to bacteria/virus inactivation and pollutant degradation. *Sci. Total Environ.* 746, 141186. <https://doi.org/10.1016/j.scitotenv.2020.141186>.
- Tao, X., Zhao, N., Yang, R., Yang, J., Cheng, X., Zhou, Y., 2020. Ultrafine Ag–Fe alloys with graphene-based cellular monolith as a novel antimicrobial material. *J. Alloy. Compd.* 816, 152592. <https://doi.org/10.1016/j.jallcom.2019.152592>.
- Tavakoli, A., Hashemzadeh, M.S., 2020. Inhibition of herpes simplex virus type 1 by copper oxide nanoparticles. *J. Virol. Methods* 275, 113688. <https://doi.org/10.1016/j.jviromet.2019.113688>.
- Tian, E., Yu, Q., Gao, Y., Wang, H., Wang, C., Zhang, Y., Li, B., Zhu, M., Mo, J., Xu, G., Li, J., 2021. Ultralow resistance two-stage electrostatically assisted air filtration by polydopamine coated PET coarse filter. *Small* 17, 2102051. <https://doi.org/10.1002/smll.202102051>.
- Valiei, A., Lin, N., Bryce, J.-F., McKay, G., Canva, M., Charette, P.G., Nguyen, D., Moraes, C., Tufenkji, N., 2020. Hydrophilic mechano-bactericidal nanopillars require external forces to rapidly kill bacteria. *Nano Lett.* 20, 5720–5727. <https://doi.org/10.1021/acsnanolett.0c01343>.

- Wang, C.C., Prather, K.A., Sznitman, J., Jimenez, J.L., Lakdawala, S.S., Tufekci, Z., Marr, L.C., 2021. Airborne transmission of respiratory viruses. *Science* 373, eabd9149. <https://doi.org/10.1126/science.abd9149>.
- Warnes, S.L., Little, Z.R., Keevil, C.W., 2015. Human coronavirus 229E remains infectious on common touch surface materials. *mBio* 6, e01697-15. <https://doi.org/10.1128/mBio.01697-15>.
- Weiss, C., Carriere, M., Fusco, L., Capua, I., Regla-Nava, J.A., Pasquali, M., Scott, J.A., Vitale, F., Unal, M.A., Mattevi, C., Bedognetti, D., Merkoçi, A., Tasciotti, E., Yilmazer, A., Gogotsi, Y., Stellacci, F., Delogu, L.G., 2020. Toward nanotechnology-enabled approaches against the COVID-19 pandemic. *ACS Nano* 14, 6383–6406. <https://doi.org/10.1021/acsnano.0c03697>.
- Wu, M.-Y., Gu, M., Leung, J.-K., Li, X., Yuan, Y., Shen, C., Wang, L., Zhao, E., Chen, S., 2021. A membrane-targeting photosensitizer with aggregation-induced emission characteristics for highly efficient photodynamic combat of human coronaviruses. *Small* 17, 2101770. <https://doi.org/10.1002/sml.202101770>.
- Ye, S., Shao, K., Li, Z., Guo, N., Zuo, Y., Li, Q., Lu, Z., Chen, L., He, Q., Han, H., 2015. Antiviral activity of graphene oxide: how sharp edged structure and charge matter. *ACS Appl. Mater. Interfaces* 7, 21571–21579. <https://doi.org/10.1021/acsmi.5b06876>.
- Zacharias, N., Haag, A., Brang-Lamprecht, R., Gebel, J., Essert, S.M., Kistemann, T., Exner, M., Mutters, N.T., Engelhart, S., 2021. Air filtration as a tool for the reduction of viral aerosols. *Sci. Total Environ.* 772, 144956 <https://doi.org/10.1016/j.scitotenv.2021.144956>.
- Zheng, K., Xie, J., 2020. Composition-dependent antimicrobial ability of full-spectrum Au_xAg_{25-x} alloy nanoclusters. *ACS Nano* 14, 11533–11541. <https://doi.org/10.1021/acsnano.0c03975>.
- Zhu, Z., Zhang, Y., Bao, L., Chen, J., Duan, S., Chen, S.-C., Xu, P., Wang, W.-N., 2021. Self-decontaminating nanofibrous filters for efficient particulate matter removal and airborne bacteria inactivation. *Environ. Sci. Nano* 8, 1081–1095. <https://doi.org/10.1039/D0EN01230K>.